C. R. Mecanique 346 (2018) 815–832

Contents lists available at ScienceDirect

Comptes Rendus Mecanique

www.sciencedirect.com

Exploring the undrained cyclic behavior of methane-hydrate-bearing sediments using CFD–DEM

Mingjing Jiang [a,b,c,*], Jun Liu [b,c], Chung Yee Kwok [d], Zhifu Shen [e]

[a] State Key Laboratory for Disaster Reduction in Civil Engineering, Tongji University, Shanghai 200092, China
[b] Key Laboratory of Geotechnical and Underground Engineering of Ministry of Education, Tongji University, Shanghai 200092, China
[c] Department of Geotechnical Engineering, College of Civil Engineering, Tongji University, Shanghai 200092, China
[d] Department of Civil Engineering, The University of Hong Kong, China
[e] Institute of Geotechnical Engineering, Nanjing University of Technology, Nanjing, China

ARTICLE INFO

Article history:
Received 4 August 2017
Accepted 28 May 2018
Available online 21 June 2018

Keywords:
Methane hydrate
Rate-dependency
CFD–DEM
Cyclic undrained shear test

ABSTRACT

Based on the mechanical experimental results of methane hydrate (MH), a bond contact model considering the rate-dependency of MH is proposed. A CFD–DEM scheme considering fluid compressibility is used to simulate a series of undrained cyclic shear tests of numerical methane-hydrate-bearing sediment (MHBS) samples. The dynamic behavior, including stress–strain relationship, dynamic shear modulus, and damping ratio, is investigated. In addition, the force chains, contact fabric and averaged pure rotation rate (APR) are examined to investigate the relationships between micromechanical variables and macromechanical responses in the DEM MH samples. The effects of temperature, confining pressure and MH saturation are also analyzed. Due to the micro-structural strengthening by the MH bonds, no obvious change in microscopic quantities is observed, and the samples remain at the elastic stage under the applied low-shear stress level. When confining pressure and MH saturation increase, the dynamic elastic modulus increases, while the damping ratio decreases. An increasing temperature (leading to weakening of MH bonds) can lower the dynamic elastic modulus, but has almost no impact on the damping ratio. On the contrary, an increasing cyclic shear stress level lowers the damping ratio, but has almost no effect on the dynamic elastic modulus.

1. Introduction

Methane hydrate (MH), a crystalline solid composed of methane and hydrogen-bonded water molecules, is formed at high ambient pressure and in low-temperature conditions prevailing along many continental margins and in the Arctic [1]. MH is viewed as one of the most promising resources due to its huge reserve potential [2–4], and increasing attention has been given to MH exploitation [5]. Compared with MHs found in continental permafrost regions, those in marine environments have attracted more attention because they are estimated to be 100 times greater in amount [6].

Marine methane hydrates generally exist in sediment sections below the seafloor, and are referred to as methane-hydrate-bearing sediments (MHBS), whose strength can be significantly improved because of the bond effect of MH [7].

* Corresponding author at: Department of Geotechnical Engineering, College of Civil Engineering, Tongji University, Shanghai 200092, China.
E-mail address: mingjing.jiang@tongji.edu.cn (M. Jiang).

https://doi.org/10.1016/j.crme.2018.05.007
1631-0721/

At the same time, MH is sensitive to the environment of the deposition zone, and the strength of MHBS may be weakened when temperature or pressure changes or under external loads. As a result, a series of significant hazards such as submarine landslide, instability of submarine pipeline, and drilling platform may occur due to failure of MHBS [8–10]. Therefore, it is crucial to study the mechanical properties of MHBS for submarine disaster prevention and MH exploitation in the future.

Some pioneering works have been carried out to investigate the mechanical properties of MHBS through a number of experimental studies on core samples in situ [11–14] or artificial samples [15–18]. For instance, Masui et al. [11] conducted triaxial compression tests on natural core samples drilled from the Eastern Nankai Through and found that shear strength and elastic modulus increase with hydrate saturation, whereas no significant tendency was observed in Poisson's ratio in relation to hydrate saturation. Li et al. [16] reported the mechanical properties of gas hydrate-bearing sediments using kaolin clay. Winters et al. [18] discovered that increasing the MH content can enhance the sediment shear strength. In addition, the mechanical properties of MHBS have also been explored by numerical methods [19–22]. These studies provide good understanding of the stress–strain responses of MHBS under different temperatures, confining pressures, strain rates, and MH saturations, etc. However, major research on the mechanical properties of methane-hydrate-bearing sediments was focused on statics analyses. Although the dynamic characteristics of MHBS have been examined by resonant column tests [23], compressional and shear wave velocity measurements [24–26] and dynamic triaxial tests [27], more studies are needed to obtain a sufficient understanding of the dynamic characteristics of MHBS. In reality, MHBS would be subject to the effects of dynamic loading, such as seismic loading and wave loading. De Alba et al. [28] showed that the random seismic load can be described by an equivalent cyclic loading of which amplitude is 65% of the peak value of seismic load and equivalent cyclic number is determined based on the earthquake magnitude. Following this widely accepted study, this paper attempts to investigate the cyclic behavior of MHBS.

Currently, it is widely accepted that the strength of MHBS depends on the microscopic distribution of MH in soils. (1) Pore filling: the hydrate nucleates in pore spaces without bridging two or more particles. (2) Cementation: the hydrate acts as a bond on the interparticle contact points. (3) Load-bearing: the hydrate grows and becomes part of the loading bearing force chain. (4) Grain-coating: the hydrate nucleates on the particle surface and can establish a cementation at contacts where the hydrate coating layers overlap [21]. Recent study by X-ray analyses reveal that the micro-structure of artificial MHBS is complicated, as the MH may exist as both loading-bearing and pore-filling matter [29]. Thus, laboratory triaxial tests on MHBS may not be capable of distinguishing the influence of micro-morphology on the mechanical properties of MHBS. The Discrete Element Method [30], on the other hand, can quantitatively describe the mechanical properties of MHBS with given micro-morphology, e.g., pore filling [19] and cementation [21]. Furthermore, MHBS may remain under undrained conditions in reality. Although the constant volume method can be used to simulate the undrained triaxial behavior of granular materials [31–33], this method may not be suitable for large boundary problems. On the other hand, the coupled CFD–DEM method has shown its significant potential in dealing with fluid-related geotechnical problems. In fact, it has been successfully applied in the analyses of fluid–particle interaction [34], liquefaction problem [35], and submarine steep-slope failures [36].

The rate-dependency of MH mechanical behavior is significant, such as the strength of MH is greatly influenced by strain rate. In one of the pioneering works by Hyodo et al. [37], the strength of MH had been shown to increase with strain rate. The same results were obtained in triaxial tests conducted by Nabeshima et al. [38]. Meanwhile, the rate-dependency of MH strength has been investigated extensively [39–41]. These researches provide good understanding of the rate-dependent behavior of MH and can help establish the DEM contact model considering the rate-dependency of MH, which constitutes the motivation of this study.

The purpose of this study is to propose a bond contact model for MHBS considering the rate dependency and investigate the dynamic behavior of MHBS under cyclic loading using the CFD–DEM scheme. Following this section, the bond contact model will be introduced, with emphasis on the rate-dependency of MH. A series of cyclic undrained shear tests are then simulated to investigate the micromechanical variables and macromechanical responses of MHBS, along with the effect of confining pressure, temperature, and saturation of MH on the dynamic behavior of MHBS under cyclic loads.

2. MH bond contact model

The bond contact model in this paper is modified from the original model in [42] for the dynamic problem. Fig. 1 illustrates a conceptual bond contact model and physical element models, which are composed of normal, tangential, and rolling contact components. These three components all include a spring reflecting an elastic behavior of the bond before failure, a bond element representing cementation at contact, and a dashpot allowing energy dissipation and quasi-static deformations. In addition, in the normal contact model, a bond element is set to be parallel with a divider in order to simulate the fact that the bond resists normal tension force, and no force is transmitted when the bond is broken and the particles separated. The tangential contact model includes a bond element in parallel with a slider that provide the bond with a shear resistance controlled by the Mohr–Coulomb criterion, even after the bond is broken. In the rolling-contact model, a bond element exists within a roller that presents bond-rolling resistance. As to the unbonded contact, the physical element models can be easily obtained by excluding the bond element in normal, tangential, and rolling components respectively.

The hydrate bond between two disks with radii R_1 and R_2 has a minimum thickness $h_{\min}$ and a maximum thickness $h_{\max}$ and a finite width $B = \overline{R}\beta^{\mathrm{b}}$, where $\overline{R} = 2R_1R_2/(R_1 + R_2)$ is the common radius and β^{b} is the rolling resistance coefficient of the bond.

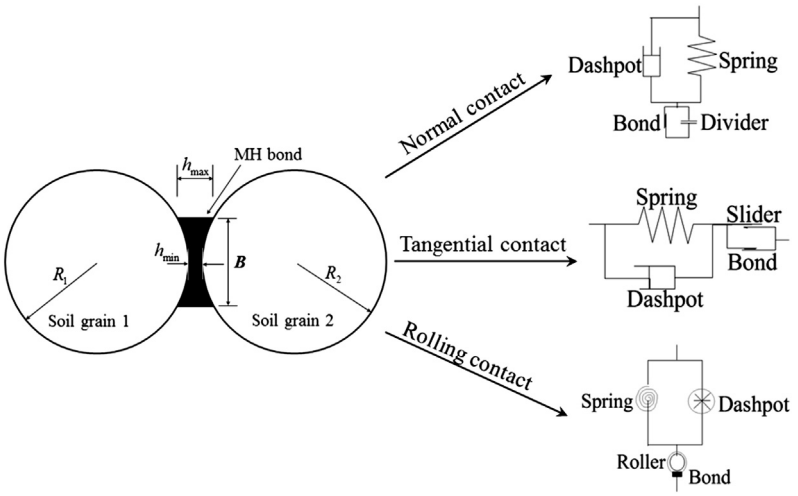

Fig. 1. Schematic illustration of methane-hydrate-bonded soil grains.

The total contact forces include the normal force F_n, the shear force F_s and the moment M, each of which is composed of the particle part (F_n^p, F_s^p, M^p) and the bond part (F_n^b, F_s^b, M^b):

$$F_n = F_n^p + F_n^b \tag{1a}$$
$$F_s = F_s^p + F_s^b \tag{1b}$$
$$M = M^p + M^b \tag{1c}$$

The mechanical responses and the bond failure criterion are described in detail in the following.

2.1. Mechanical responses

Fig. 2 illustrates the mechanical responses of the bonded contact, where K_n^b, K_s^b, and K_r^b are the normal, tangential, and rolling stiffness of the bond respectively; u_n^b, u_s^b, and θ^b are the translational displacement, the tangential displacement, and the rotation angle of the bond, respectively; λ and μ^b are the residual strength coefficient of the bond and the friction coefficient of the bond, respectively.

It can be observed in Fig. 2 that the compressive force, the tensile force, the shear force, and the moment transmitted by the bonded contact all increase linearly with the increase of the corresponding displacement/moment up to a limit value, i.e. the bond tensile resistance R_t^b, the bond compressive resistance R_c^b, the bond shear resistance R_s^b, and the bond rolling resistance R_r^b, respectively. Then the compressive force, the shear force, and the moment reduce to their residual values as a result of bond breakage, except that the tensile force drops to zero.

After the bond breaks, the interaction at a physical contact without bond material is described by an unbonded contact law. The mechanical responses of the unbonded inter-particle contact are shown in Fig. 3, where K_n^p, K_s^p, and K_r^p are the normal, tangential, and rolling stiffness of the particle, respectively; u_n^p, u_s^p, and θ^p are the translational displacement, the tangential displacement, and the rotation angle of the particle, respectively; μ^p and β^p are the friction coefficient of the particle and the rolling resistance coefficient of the particle, respectively. Compared with the previous static bond contact model [42,43], a distinct feature is that different normal stiffness values for loading and unloading are used in the unbonded contact model to account for a dynamic problem; this is one of the dynamic features in this model. In addition, linear viscous damping was used to dissipate kinematic energy. The normal, tangential, and rotational viscous damping forces/moment can be calculated as:

$$F_n^v = c_n \dot{u}_n \tag{2a}$$
$$F_s^v = c_s \dot{u}_s \tag{2b}$$
$$M^v = c_r \dot{\theta} \tag{2c}$$

where c_n, c_s, and c_r are the normal, tangential, and rotational viscous damping coefficients, respectively; $\dot{u}_n$, $\dot{u}_s$, and $\dot{\theta}$ are the normal, tangential, and rotational rates, respectively. The damping coefficients can be calculated by:

$$c_n = r_n c_n^{crit} \tag{3a}$$
$$c_s = r_s c_s^{crit} \tag{3b}$$

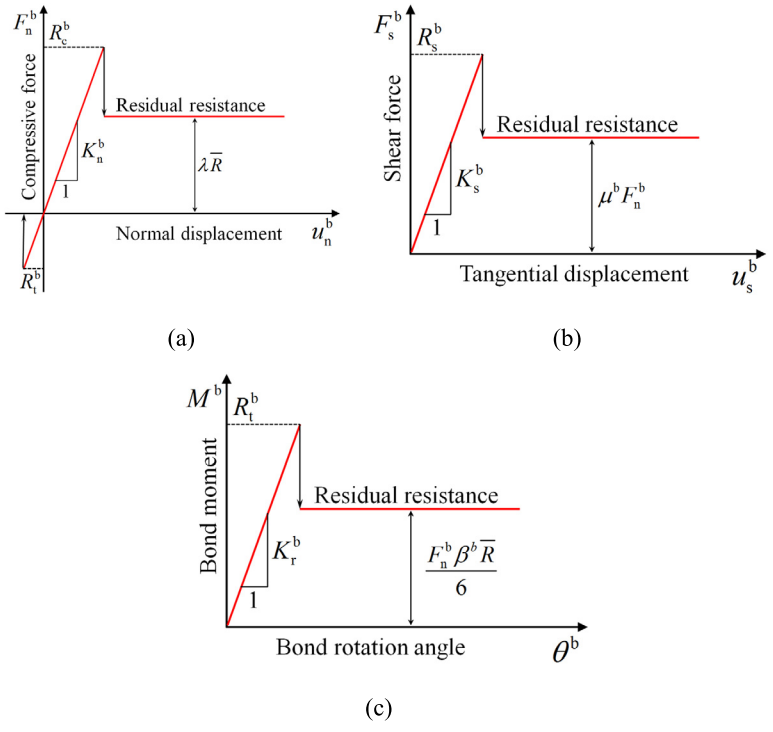

Fig. 2. The mechanical responses of the bonded contact: (a) normal direction; (b) tangential direction; (c) rolling direction.

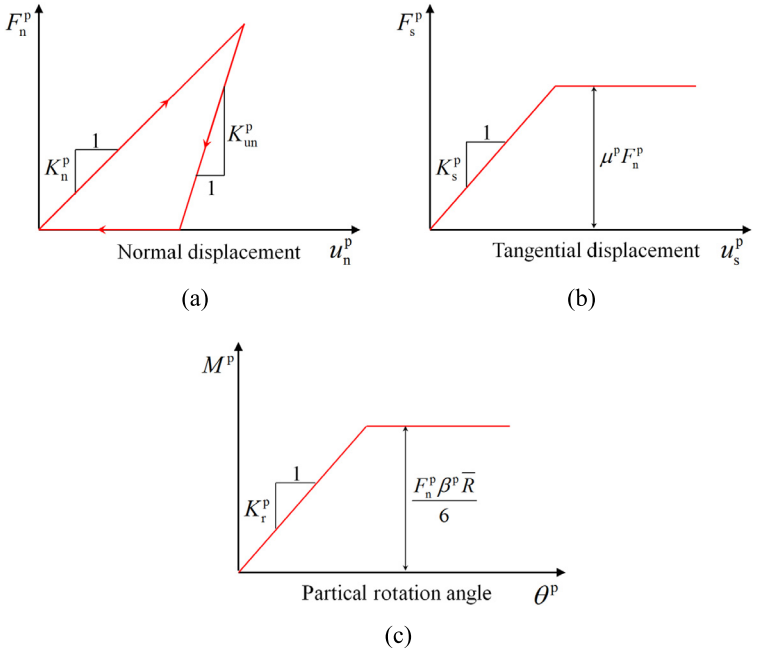

Fig. 3. Mechanical response of particle contacts in (a) normal direction, (b) tangential direction, and (c) rolling direction.

$$c_{\mathrm{r}} = \left(\bar{R}\beta^{\mathrm{p}}\right)^2 c_{\mathrm{n}}/12 \tag{3c}$$

where r_{n} and r_{s} are two parameters, and $c_{\mathrm{n}}^{\mathrm{crit}}$ and $c_{\mathrm{s}}^{\mathrm{crit}}$ are the normal and tangential critical damping constants:

$$c_{\mathrm{n}}^{\mathrm{crit}} = 2\sqrt{mK_{\mathrm{n}}^{\mathrm{p}}} \tag{4a}$$

$$c_{\mathrm{s}}^{\mathrm{crit}} = 2\sqrt{mK_{\mathrm{s}}^{\mathrm{p}}} \tag{4b}$$

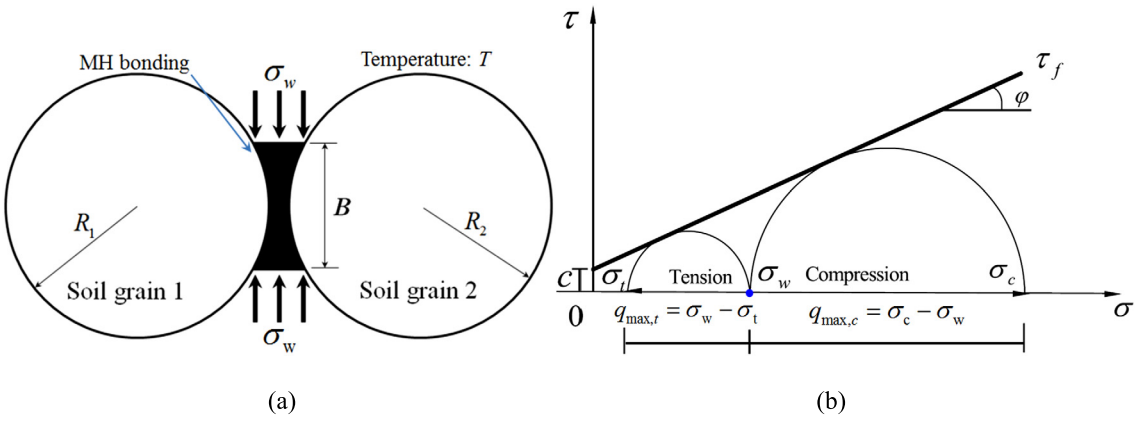

Fig. 4. Sketch of: (a) two MH bonded granules and (b) shear strength envelope of pure MH.

where m is the effective system mass, which is the disc mass in the case of a disc–wall contact, or is equal to $m_1 m_2/(m_1 + m_2)$ in the case of a disc–disc contact (m_1 and m_2 are masses of the two discs).

2.2. Bond-failure criterion

Whether a bond will break is determined by a failure criterion derived from a series of micromechanical tests on idealized bonded granular materials [44,45]. A MH bond can break under a combination of a normal force F_n (in tension or compression), a shear force F_s, and a rolling moment M. The bond failure criterion can be written as:

$$\left(\frac{F_s^b}{R_s^b}\right)^2 + \left(\frac{M^b}{R_r^b}\right)^2 \begin{cases} < 1, & \text{intact bond} \\ = 1, & \text{critical state} \\ > 1, & \text{broken bond} \end{cases} \tag{5}$$

According to Jiang et al. [44,45], the bond resistances including R_s^b, R_r^b, R_c^b, and R_t^b are determined as follows:

$$R_s^b = f_s \times g_s \times \left(F_n^b + R_t^b\right) \times \left[\ln\left(\frac{R_c^b + R_t^b}{F_n^b + R_t^b}\right)\right]^{0.59} \tag{6a}$$

$$R_r^b = f_r \times g_r \times \left(F_n^b + R_t^b\right) \times \left[\ln\left(\frac{R_c^b + R_t^b}{F_n^b + R_t^b}\right)\right]^{0.59} \tag{6b}$$

$$R_t^b = B \times q_{max,t} \tag{6c}$$

$$R_c^b = B \times q_{max,c} \tag{6d}$$

where $f_s = 2.05\text{–}0.89 \times e^{-(1000 h_{min} - 1.15)^2}$, $f_r = 2.05 - 0.92 \times e^{-(1000 h_{min} - 1.15)^2}$, $g_s = 0.41\text{–}61.07 h_{min}$ and $g_r = 0.83\text{–}146.36 h_{min}$ are fitting parameters based on experimental results [44,45].

Fig. 4 provides a sketch of two MH bonded granules at temperature T and the surrounding water pressure σ_w, along with the shear strength envelope of pure MH, having assumed the validity of the Mohr–Coulomb failure criterion, where σ_t and σ_c are the minimum and maximum principal stresses, respectively. Depending on the value of water pressure, σ_t may be tensile. Thus, $q_{max,c}$ and $q_{max,t}$ can be expressed as:

$$q_{max,t} = \sigma_w - \sigma_t \tag{7a}$$

$$q_{max,c} = \sigma_c - \sigma_w \tag{7b}$$

Triaxial compression tests on pure MH bulk sample show that the shear strength of MH q_{max} depends on temperature, confining pressure, sample density, and strain rate [37,38,46–48]. The first three factors have been discussed and incorporated into the previous static bond contact model and applied in DEM simulations [42,43]. This study further accounts for the strain rate effect. Fig. 5 shows that the peak shear strength of MH increases with the logarithm of the axial strain rate in an almost linear way. The peak strength of MH q_{max} (MPa) was fitted and implemented into the dynamic bond contact model:

$$q_{max} = q_{max}^*(T, \sigma_w) + \xi \log \dot{\varepsilon}_1 \tag{8}$$

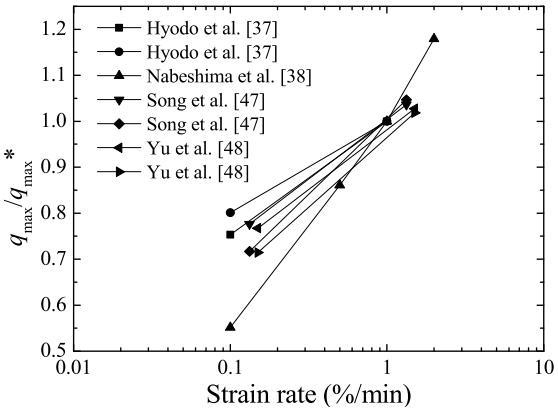

Fig. 5. Rate-dependency of MH strength.

where $q^*_{\max}(T, \sigma_w)$ (MPa) is the peak shear strength when the axial strain rate $\dot{\varepsilon}_1$ is 1%/min, which depends on σ_w and T. The parameter ξ (MPa) is not a constant, but depends on σ_w and T:

$$\xi = a\sigma_w\left(\frac{T}{T^*} + b\right) \tag{9}$$

where $T^* = 273$ K and the fitting parameters $a = -3.7$, $b = -1.0$. In this fitting equation, σ_w is in MPa and T is in K.

Based on Eqs. (8) and (9), the peak strength of MH under various strain rates can be obtained, which is used to determine the bond resistances in Eqs. (6c) and (6d). In this way, the temperature, pore pressure, density [42] and strain-rate-dependent bond resistances are considered in a consistent way. This is another dynamic feature in this model.

2.3. Governing equations for fluids

The CFD governing equations for fluids are given in Eqs. (10)–(11), where n is porosity; ρ^f is fluid density, which is not constant during the simulation, unlike in the classical CFD–DEM; $\mathbf{U}^f$ is the average velocity of a fluid cell; p is the fluid pressure in the cell; μ^f is the viscosity coefficient of the fluid; $\mathbf{F}^p$ is the interaction force the particles inside the cell exert on the fluid; $\mathbf{g}$ is the gravitational acceleration. It should be noted that there are four variables in the governing equations, and to determine the four variables, a fluid state equation has to be considered. As illustrated in Eq. (12), Li [49] proposed a state equation for seawater, and the equation is chosen in this study. In Eq. (12), ρ_f and ρ_{f_0} are fluid density and the initial fluid density, S is salinity of sea water, T is the temperature, P and P_0 are fluid pressure and the initial fluid pressure, and A, C and A^* are fitting parameters decided by Eqs. (12). The units of A and A^* are 10^5 Pa = 1 bar.

$$\frac{\partial(n\rho^f)}{\partial t} + \nabla\cdot\left(n\rho^f\mathbf{U}^f\right) = 0 \tag{10}$$

$$\frac{\partial(n\rho^f\mathbf{U}^f)}{\partial t} + \nabla\cdot\left(n\rho^f\mathbf{U}^f\mathbf{U}^f\right) = -\nabla p - \mathbf{F}^p + n\rho^f\mathbf{g} + n\nabla\cdot\left(\mu^f\nabla\mathbf{U}^f\right) \tag{11}$$

$$\begin{cases} \dfrac{\rho_f - \rho_{f_0}}{\rho_f} = \left(1 - S\times 10^{-3}\right)C\log\left(\dfrac{A^* + P}{A^* + P_0}\right) \\ A = 2668 + 19.867T - 0.311T^2 + 0.001778T^3 \\ C = 0.315 \\ A^* = (2670 + 6.89656\times S) + (19.39 - 0.0703178\times S)T - 0.223T^2 \end{cases} \tag{12}$$

3. CFD–DEM coupling scheme

The basic coupling principle is that the particle–fluid interactions are considered in addition to particle–particle interactions in DEM and fluid–fluid interactions in CFD. In this coupling scheme, the pressure-gradient force and the drag force are considered as the interaction forces between fluid and particles. In a fluid cell, the pressure-gradient force can be calculated by:

$$\mathbf{F}_p = -\nabla\mathbf{p}\sum_{i=1}^{n_p} V_p^i \tag{13}$$

where $\mathbf{p}$ is the hydraulic pressure, n_p is the particle number in the fluid cell, and V_p^i is the volume of particle i.

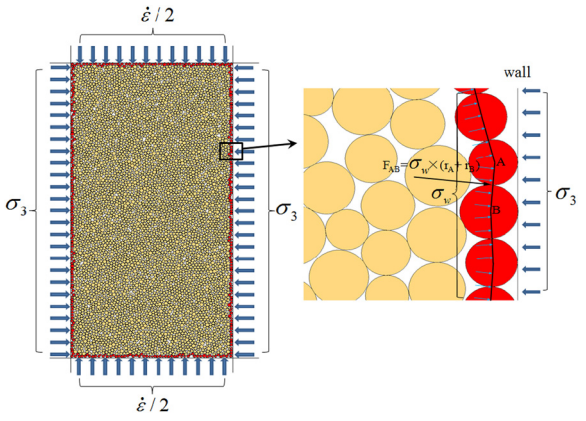

Fig. 6. Sample and schematic of loading.

Due to the complex particle configuration, there is no accurate theoretical solution for the drag force. Two empirical formulas based on the bed pressure drop tests [50,51] are used:

$$\mathbf{f}_{\text{drag}} = (1-n)\left(150\frac{\mu^{\text{f}}(1-n)}{n\bar{d}_{\text{p}}^2} + 1.75\frac{\rho^{\text{f}}|\mathbf{u}_{\text{f}} - \bar{\mathbf{u}}_{\text{p}}|}{\bar{d}_{\text{p}}^2}\right)(\mathbf{u}_{\text{f}} - \bar{\mathbf{u}}_{\text{p}}), \quad n > 0.8 \tag{14}$$

$$\mathbf{f}_{\text{drag}} = 0.75(1-n)\left(\frac{C_{\text{D}}Re^{-265}\mu^{\text{f}}\rho^{\text{f}}|\mathbf{u}_{\text{f}} - \bar{\mathbf{u}}_{\text{p}}|}{\bar{d}_{\text{p}}}\right)(\mathbf{u}_{\text{f}} - \bar{\mathbf{u}}_{\text{p}}), \quad n \le 0.8 \tag{15}$$

where C_{D} is the drag coefficient, calculated by Eq. (16) [51], $\bar{d}_{\text{p}}$ is the average diameter of particles in a fluid cell, $\mathbf{u}_{\text{f}}$ and $\bar{\mathbf{u}}_{\text{p}}$ are the fluid velocity vector and the average particle velocity vector, respectively. Re is the Reynolds number and can be obtained by Eq. (17) [51].

$$C_{\text{D}} = \begin{cases} \dfrac{24}{Re}\left(1 + 0.15Re^{0.687}\right), & Re \le 1000 \\ 0.44, & Re > 1000 \end{cases} \tag{16}$$

$$Re = n\rho^{\text{f}}\bar{d}_{\text{p}}|\mathbf{u}_{\text{f}} - \bar{\mathbf{u}}_{\text{p}}|/\mu^{\text{f}} \tag{17}$$

Pore pressures and fluid velocities are solved in CFD, while the forces between particles and particle velocities are calculated in DEM. When the coupling is started, the pore pressure, fluid velocities, forces between particles, and particle velocities are passed to the coupling module to obtain the porosity, drag force and interactive force between the fluid and the particles. Then the drag force and porosity are passed to the CFD, and the interactive force between fluid and particles are passed to the DEM.

4. CFD–DEM analysis of undrained cyclic shear tests on MHBS

The bond contact model was implemented by the C++ code into the DEM software PFC2D for the simulation of cyclic shear tests through the proposed CFD–DEM scheme. The simulations were carried out in four steps: (1) generation of unbonded sample without MH cementation; (2) activation of MH bonds in the sample; (3) isotropic compression; (4) cyclic shearing of the samples. During cyclic loading, the sample was sheared at a strain rate of 1%/min and the shear directions of the loading walls were reversed when the deviator stress reached the target value. The lateral load is servo-controlled to keep the total confining pressure constant.

The homogeneous unbonded sample consisting of 6000 particles at a target void ratio of 0.25 was generated by the Multi-layer with Undercompaction Method (UCM) proposed by Jiang et al. [52], with a maximum, a minimum, and a mean diameter of 9 mm, 6 mm, and 7.8 mm. The void ratio of 0.25 corresponds to a dense sample. The uniformly coefficient is 1.3. The sample was then subjected to an effective confining pressure of 0.2 MPa. Then, the MH bonds were activated. Fig. 6 illustrates the DEM sample with a width of 400 mm and a height of 800 mm, and the enlarged part of the sample in Fig. 6 illustrates the pore pressure, as will be discussed later.

After the sample was prepared, the sample was consolidated under the effective confining pressure of 1, 2, and 3 MPa, respectively. Then the sample was cyclically sheared under a constant strain rate of 1%/min, which means that when the vertical stress reached the target value in one direction, the load was applied in an inverse direction. The target stress value was controlled by the cyclic stress amplitude q_{cyc}, referring to [53], the dynamic stress ratio was set as 0.3. q_{cyc} was assigned two values in the simulations: $q_{\text{cyc,sand}} = 5/6q_{f,\text{sand}}$ and $q_{\text{cyc,MHBS}} = 5/6q_{f,\text{MHBS}}$, where $q_{\text{cyc,sand}}$ is the dynamic

Table 1
Particle and fluid parameters in the CFD–DEM analyses.

Material parameter	Value
Particle density	2650 kg/m^3
K_n^p	6×10^8 N/m
K_s^p	4×10^8 N/m
K_m^p	$K_n^p(\beta^p\overline{R})^2/12$
μ^p	0.5
β^p	0.5
K_n^p/K_{un}^p	0.95
K_n^b	Eq. (14)
K_s^b	$2K_n^b/3$
K_r^b	$K_m^p(\beta^p\overline{R})^2/12$
R_s^b	Eq. (6a)
R_r^b	Eq. (6b)
R_t^b	Eq. (6c)
R_c^b	Eq. (6d)
μ^b	0.5
Normal stiffness between particles and wall	6.0×10^8 N/m
Tangential stiffness between particles and wall	4.0×10^8 N
Friction coefficient of wall	0.0
Initial fluid density	1000 kg/m^3
Fluid viscous coefficient	0.001 Pa s

stress amplitude of pure sand (no MH bond), and $q_{cyc,MHBS}$ is the dynamic stress amplitude of MHBS. $q_{f,sand}$ is the shear strength of pure sand and $q_{f,MHBS}$ is the shear strength of MHBS ($q_{f,MHBS} > q_{f,sand}$) in the biaxial monotonic test.

The pore fluid pressure was applied on the outermost layer particles (red particles in Fig. 6) which was counter-balanced by the wall. In this way, the stress on the wall is the total stress. Taking particles A and B, for example, the resultant force $F_{AB} = p(r_A + r_B)$ is shared by particles A and B:

$$F_A = F_{AB}\frac{r_A}{r_A + r_B} \tag{18}$$

$$F_B = F_{AB}\frac{r_B}{r_A + r_B} \tag{19}$$

In DEM, the lateral boundary walls maintained a constant total stress by a servo-mechanism. The top and bottom boundaries were moved at a strain rate of 1%/min. To maintain the compatibility of CFD and DEM geometries, the fluid in CFD was assigned the same velocity as the wall along the sample's boundary, and no flow is allowed.

4.1. Sample parameters

Table 1 summarizes the parameters of particles, bond material, and fluid used in this study. The parameters of the unbonded part, i.e. the particle contact stiffness parameters, rolling resistance coefficient, along with the particle friction coefficient, are selected based on a previous study [42]. These parameters are determined by trial-and-error and are chosen to match the mechanical behavior of the host sand in triaxial compression tests. As to the bonded part, since the Young's modulus for soil grains ranges from 50 to 70 GPa. They can be regarded as rigid particles when the bonds (e.g., MH bonds) have a lower elastic modulus. As illustrated in Fig. 1, for the case of rigid particles with a deformable elastic bond, the normal deformation of the bond material, δ_n, can be expressed as

$$\delta_n = \varepsilon t = \frac{\sigma t}{E} = \frac{F_n t}{BE} \tag{20}$$

where ε is the normal strain, σ is the evenly distributed normal stress, E is Young's modulus of the bonding material and t is the average thickness of the bonding material. Thus, the normal contact stiffness of bond can be related to E as follows:

$$K_n^b = \frac{F_n}{\delta_n} = \frac{BE}{t} \tag{21}$$

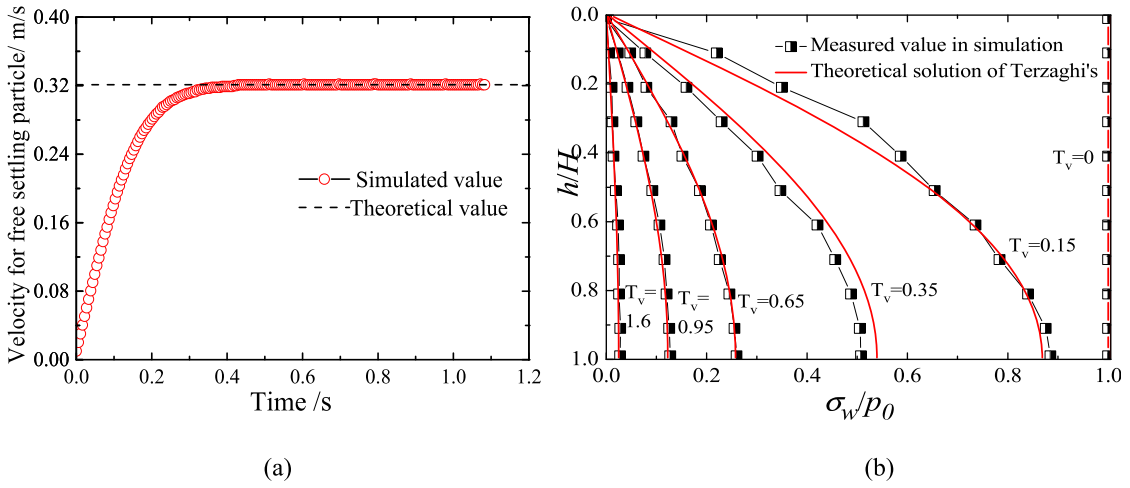

Fig. 7. Comparison of the CFD–DEM prediction and analytical solution for: (a) single particle settling, and (b) one-dimensional consolidation tests.

Experimental data obtained from tests on pure MHs [46] reveal that E is strongly related with the temperature T, the confining pressure (i.e. the pore pressure in this case, σ_w), and MH density ρ. By fitting experimental data [46], E can be inferred using:

$$\frac{E}{p_a} = 3\left(\frac{\sigma_w}{p_a}\right) - 1.98\left(\frac{T}{T_0}\right) + 4950.50\left(\frac{\rho}{\rho_w}\right) - 1821.78 \tag{22}$$

The tangential and rolling bond contact stiffness values can be assumed to be proportional to the normal contact stiffness, with the former one determined by experimental investigations [44,45] and the latter one determined by the assumption of elastic bond [54]:

$$K_s^b = \frac{2}{3}K_n^b \tag{23}$$

$$K_r^b = \frac{1}{12}K_n^b B^2 \tag{24}$$

In this study, the MH has a density of 0.9 g/cm^3 to match the experimental conditions [46]. The stiffness ratio K_n^p/K_{un}^p is set to 0.95 based on the analysis by Thornton et al. [55]. Other parameters have been calibrated in our previous study [36], in which the CFD–DEM prediction and analytical solution for single-particle settling and one-dimensional consolidation tests are compared, as illustrated in Fig. 7. During the simulation, the salinity S is set to the mean value of seawater 3.5%. The tangential damping ratio r_s is the same as the normal damping ratio r_n, and r_n can be obtained by:

$$r_n = \frac{\ln e}{\sqrt{(\ln e)^2 + \pi^2}} \tag{25}$$

where e is the reconstitution coefficient that can be obtained from drop tests [56].

Fig. 8 illustrates the DEM sample after consolidation and the CFD griding. By trial, it is reasonable that a grid contains 8–20 particles. The colored particles are merely to improve the visualization and the 15 × 30 grids are set in the CFD module, with each grid size of 26 mm × 26 mm and each grid contains about 12 particles. The analysis showed that the difference of pore pressure in the sample is very small, so the pore pressure is calculated using the mean value of each cell.

4.2. Scheme of the simulation

The simulations are divided in three groups labeled with T01, T02 and T03 to investigate the effects of temperature, MH saturation, and effective confining pressure on the dynamic mechanical properties of MHBS, as shown in Table 2. Each group is subjected to two different dynamic stress amplitudes, i.e. $q_{cyc,sand} = 5/6q_{f,sand}$ and $q_{cyc,MHBS} = 5/6q_{f,MHBS}$.

Before testing MHBS, a series of undrained cyclic triaxial tests on pure sand were conducted and compared with experimental results [57]. The test condition of the pure sand was the same as T01, except that MH was not considered and $q_{cyc} = q_{cyc,sand}$. Fig. 9 illustrates the stress–stain relationship and the effective stress paths obtained in simulation and in laboratory experiments. Fig. 9 shows a qualitative consistency between the simulation results and experimental ones. Liquefaction will occur after about 20 loading cycles, indicating that the coupling scheme is capable of capturing the shear behavior of sand under undrained cyclic triaxial test. Note that the undrained behavior of sand depends on initial void ratio, dynamic stress amplitude, and loading rate, etc., and the same DEM sample as in a previous study [42] was used in this study. Thus, only qualitative comparison was made.

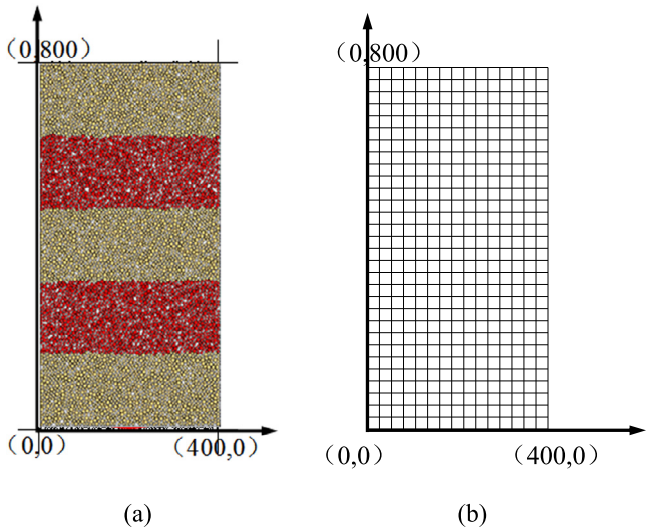

Fig. 8. (a) Consolidated DEM sample and (b) the CFD griding.

Table 2
Scheme of the simulation.

Test number	Temperature (K)	MH saturation (%)	Effective confining pressure (MPa)
T01	283	25	1, 2, 3
T02	268, 274, 283	25	1
T03	283	25, 30, 40, 50	1

5. Simulation results

Because the shear responses of MHBS under different temperatures, effective confining pressures, and saturations are similar, only the results under one condition with an effective confining pressure of 1 MPa, a temperature of 283 K, a MH saturation of 25%, and an initial pore pressure of 10 MPa are presented in detail. The macroscopic responses of MHBS under $q_{\mathrm{cyc,sand}}$ are presented and compared with the simulation results of pure sands. Then the simulation results on MHBS under $q_{\mathrm{cyc,sand}}$ are discussed with emphasis on the stress–strain relationship, E_{d} and λ_{d} to investigate the dynamic behavior of MHBS from a microscopic view. The dynamic shear modulus E_{d} and damping ratio λ_{d} are the main indexes in the stress–strain relationship of geotechnical material under cyclic loads and can be utilized in earthquake analysis and field safety assessment. Fig. 10 presents the typical hysteretic loop in the stress–strain relationship of geotechnical material under cyclic loads. The loop area represents energy consumption during the loading and unloading process and the damping ratio λ_{d} is also related to the loop area. The mean slope of the loop is denoted by E_{d}. E_{d} and λ_{d} are calculated by:

$$E_{\mathrm{d}} = \frac{q_{\max}}{\varepsilon_{\max}} \tag{26}$$

$$\lambda_{\mathrm{d}} = \frac{A_{\mathrm{L}}}{4\pi A_{\mathrm{T}}} \tag{27}$$

where $q_{\max}$ is the maximum deviator stress, $\varepsilon_{\max}$ is the maximum axial strain, A_{L} is the area of hysteretic loop in the q–ε_{a} plane, and A_{T} is the area of the triangle in Fig. 8.

Finally, the effects of temperature, MH saturation and effective confining pressure on the dynamic behavior of MHBS are discussed. Note that the focus is on the bond effect of MH, thus the temperature is assumed to only change the properties of the MH bond, while the fluid's properties are unaffected.

5.1. Macroscopic mechanical response of MHBS

Fig. 11 illustrates the stress–strain relationship and the effective stress path of MHBS during cyclic shearing. It shows that the stress–strain relationship and the effective stress path are like hysteretic loops after one cyclic load. The closed curves in Fig. 11 show that, unlike the undrained cyclic triaxial test on pure sand, in which liquefaction will occur after about 20 loading cycles, the MHBS samples are in elastic stages during cyclic loading as a result of the bonding effect of MH.

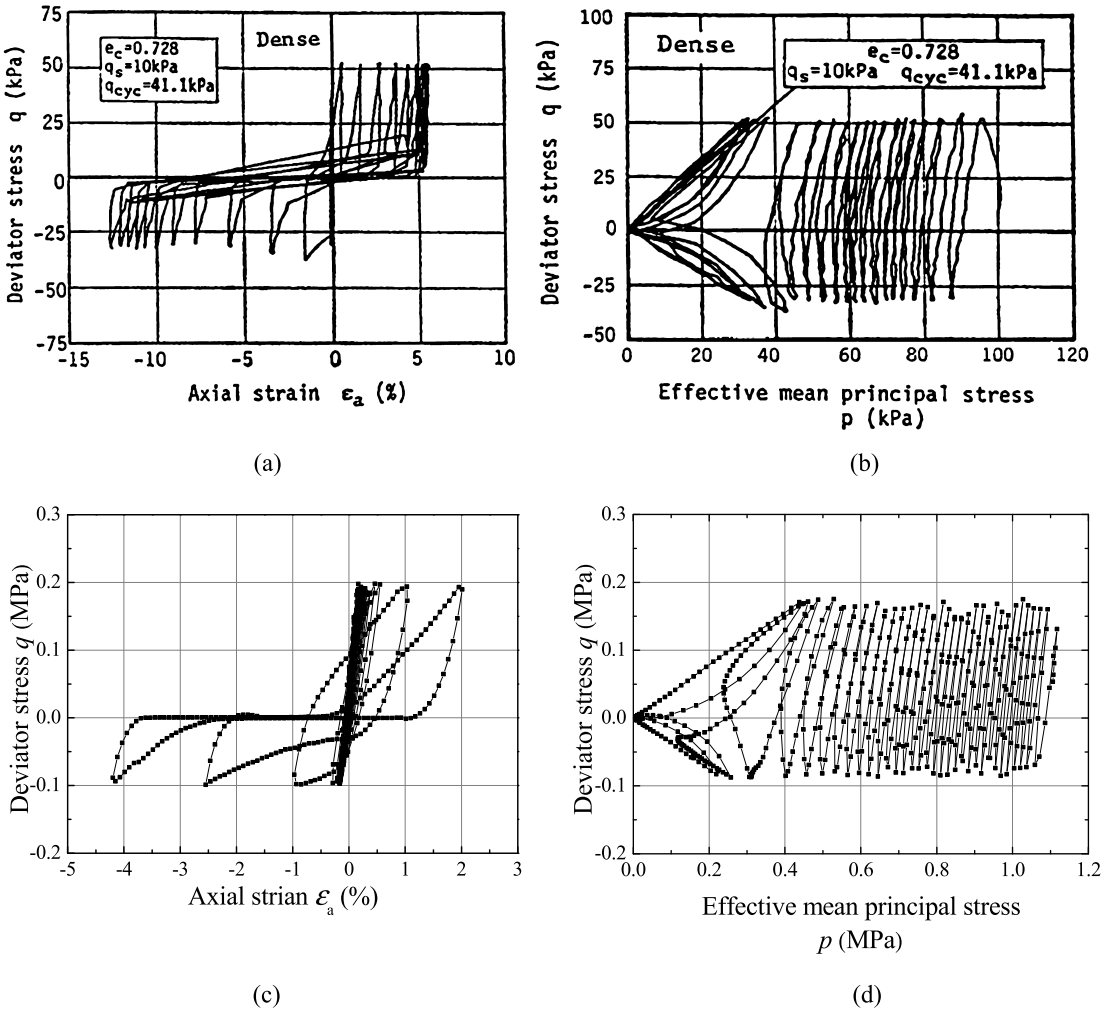

Fig. 9. Comparison of simulation and experimental results [57] on pure sand: (a) stress–strain relationship in laboratory, (b) effective stress path in laboratory, (c) stress–strain relationship in simulation, and (d) effective stress path in simulation.

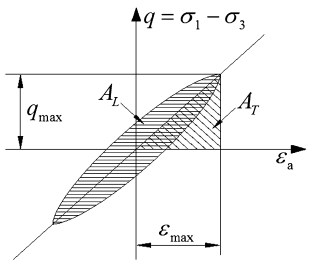

Fig. 10. Hysteretic loop in cyclic loading.

5.2. Microscopic response of MHBS

To investigate the microscopic features of MHBS during cyclic loading, the force chains, contact fabric, and average pure rotation (APR) of the MHBS sample at given moments in Fig. 12 will be analyzed in the following. Four moments, which are represented by points O, A, B, and C in Fig. 12, are used.

As illustrated in Fig. 13, force chain is shown by representing each normal contact force with a line connecting the centers of the two contacted granules with the line thickness representing the magnitude of the force. Thicker force chains refer to stronger particle contact forces. In addition, the black force chains mean compressive contact forces, and red chains are tensile. Note that the sizes of MHBS at different moments are presented as the same for clear comparison. Fig. 13 shows

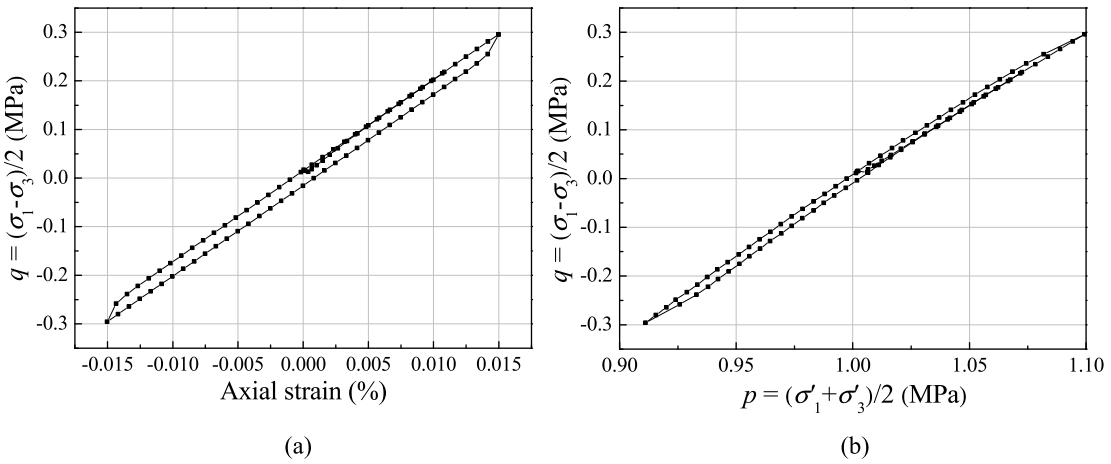

Fig. 11. Macroscopic mechanical responses of MHBS: (a) stress–strain relationship of MHBS and (b) effective stress path of MHBS.

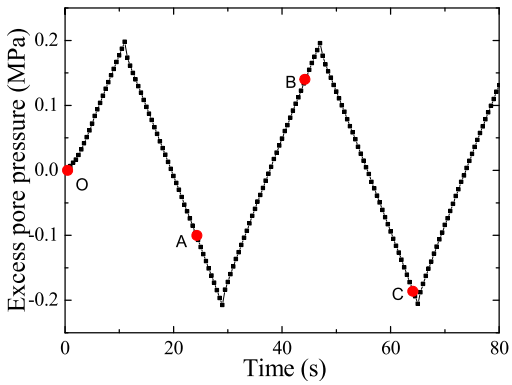

Fig. 12. Variation of excess pore pressure against time and the positions of the typical moments during the simulation.

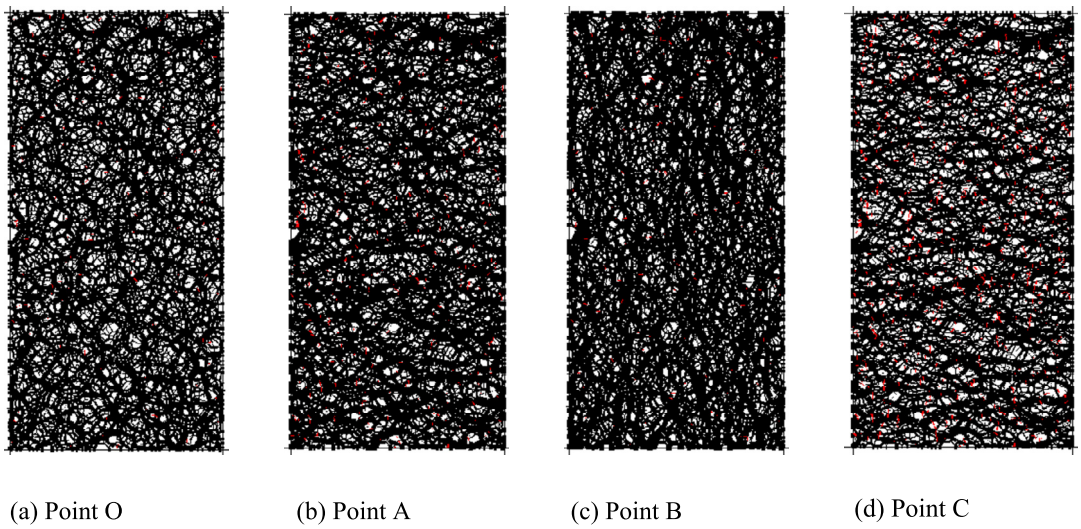

Fig. 13. Distribution of force chains of MHBS at different moments.

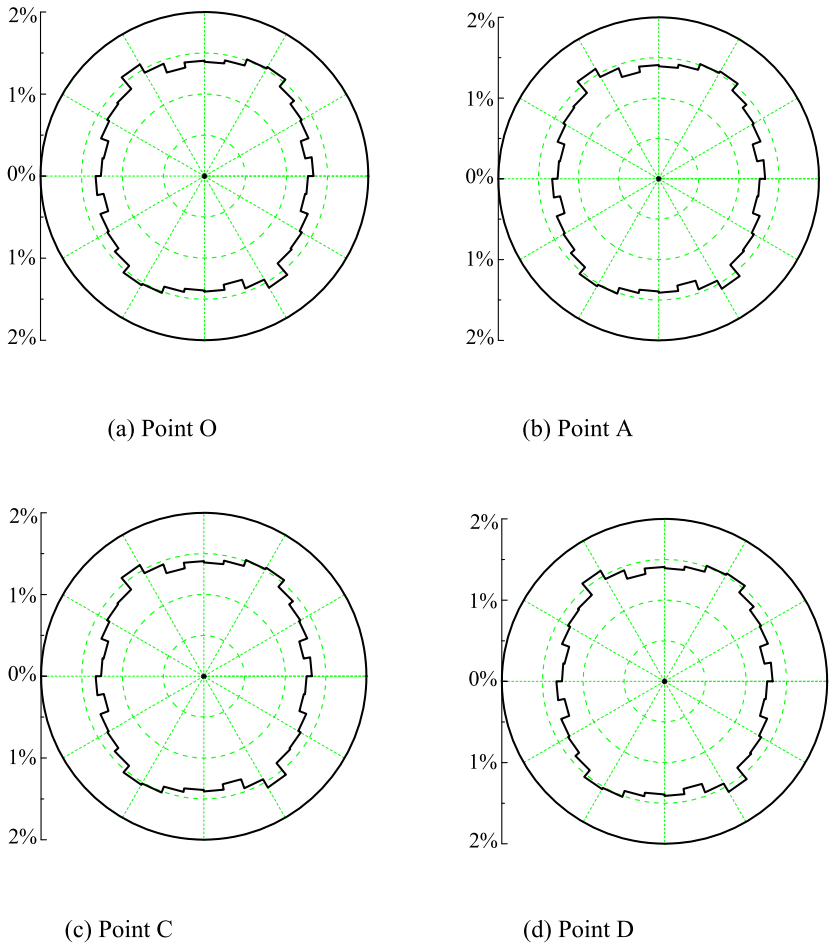

Fig. 14. Contact fabric of MHBS at different moments.

that the force chains are mainly vertically and horizontally distributed and except for the initial state (point O), at which the force chains are uniformly distributed in the sample. The distribution of the force chains changes with the loading direction. Meanwhile, regions with very few and weak force chains emerge at point C, showing that relatively fewer contact forces are transferred by the particles. However, no liquefaction occurs as a result of the bonding of MH.

Fig. 14 provides the contact fabric of MHBS at different moments, it can be observed that the contact fabric seldom changed during cyclic loading, which is caused by the MH bonding that restricts the movement of particles. As to the particle rotation, Fig. 15 illustrates the distributions of average pure rotation rate (APR). The APR is proposed by Jiang et al. [58] and could be used as one of the kinematic characteristics of granules during loading. Fig. 15 shows that despite slightly variations, the APR is evenly distributed in the sample during cyclic loading. Overall, the microscopic characteristics of MHBS sample during cyclic loading seldom changed as a result of MH bonding.

5.3. The influence of test conditions on the dynamic behavior of MHBS

This section investigates the influence of temperature, saturation of MH and effective confining pressure on the dynamic behavior of MHBS under $q_{\mathrm{cyc,sand}}$ and $q_{\mathrm{cyc,MHBS}}$.

5.3.1. The influence of temperature

Fig. 16 illustrates the effect of temperature on the dynamic mechanical properties of MHBS. E_{d} almost decreases linearly while λ_{d} only slightly varies with increasing temperature. The values of E_{d} and λ_{d} under $q_{\mathrm{cyc,sand}}$ are larger than that under $q_{\mathrm{cyc,MHBS}}$ at the same temperature.

Fig. 17 illustrates the evolution of the mean strain rate of MH bond with the temperature. The mean strain rate is the average value of the maximum and minimum strain rates during shearing. When temperature increases, both the mean normal and tangential strain rates of MH bond slightly increase with increasing temperature. The mean normal strain rate is larger than the tangential one, and the shear stress amplitude seldom affects the mean strain rate. The viscous energy consumed during cyclic shearing is determined by the strain rate of MH bond. Thus, it can be concluded that during

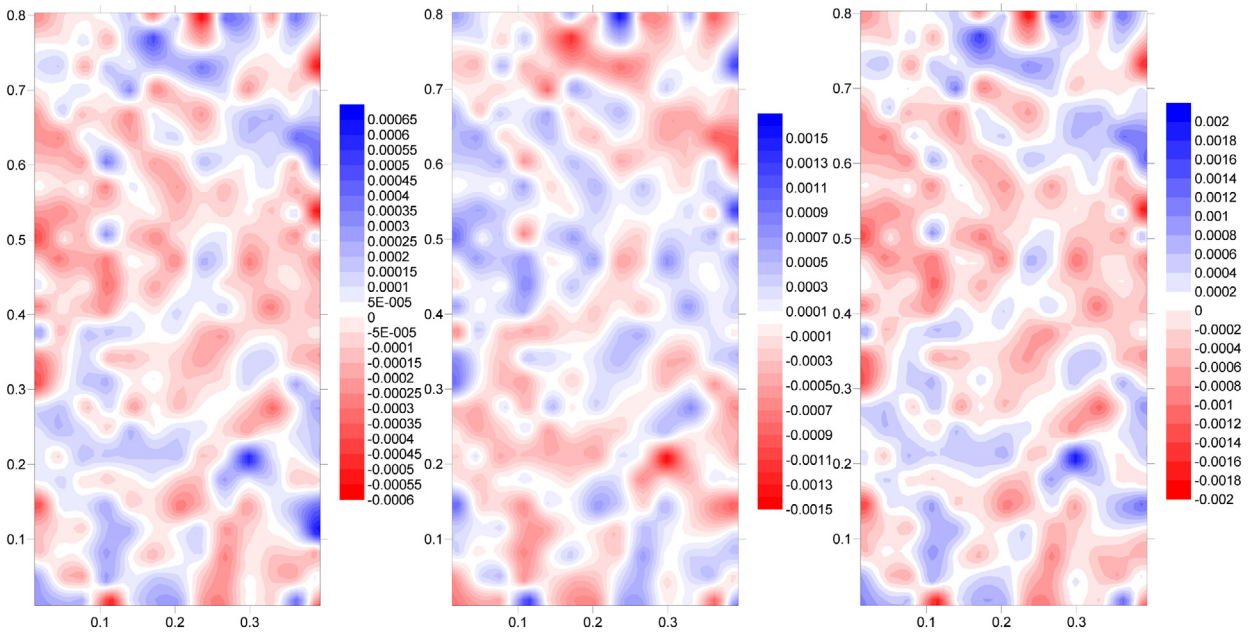

Fig. 15. Distributions of the APR at different moments.

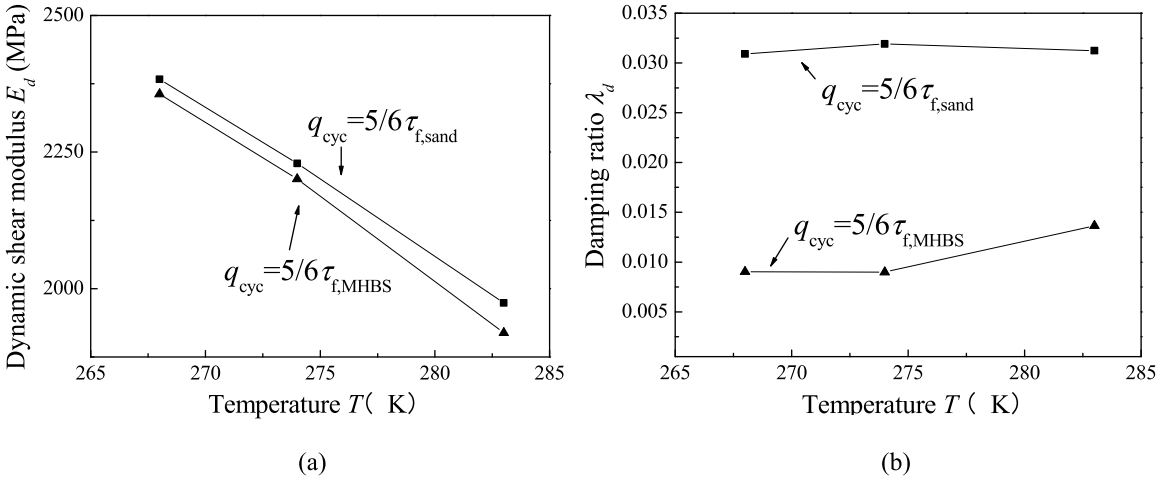

Fig. 16. Influence of different T values on (a) E_d and (b) λ_d.

undrained cyclic triaxial tests of MHBS, the viscous energy is mainly consumed in the normal direction of grain contact. Increasing the temperature and stress amplitude seldom affects the mean strain rate and, as a result, the temperature has only a slight effect on the damping ratio in Fig. 17.

5.3.2. The influence of MH saturation

MH saturation of in this paper can be calculated from the geometry of all the bonds in the sample, see [42]:

$$S_{MH} = \frac{A_b}{A_v} + S_{MH_0} = \frac{(1+e_p)}{e_p A}\sum_{i=1}^{m} A_{b,i} + S_{MH_0}$$
$$= \frac{(1+e_p)}{e_p A}\sum_{i=1}^{m} \bar{R}_i^2\left[2\beta^b - \beta\sqrt{1-\frac{(\beta^b)^2}{4}} - 2\arcsin\left(\frac{\beta^b}{2}\right) + \frac{t_{0i}\beta^b}{\bar{R}_i}\right] + S_{MH_0} \tag{28}$$

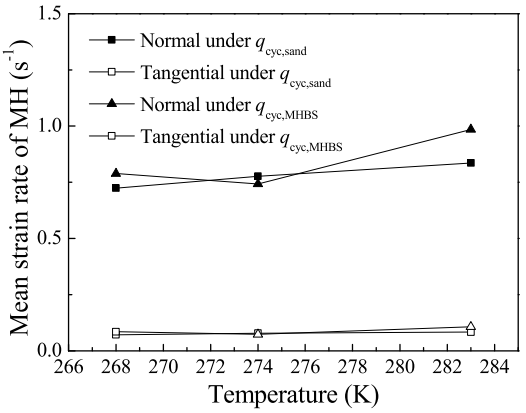

Fig. 17. Mean strain rate of MH under different temperatures.

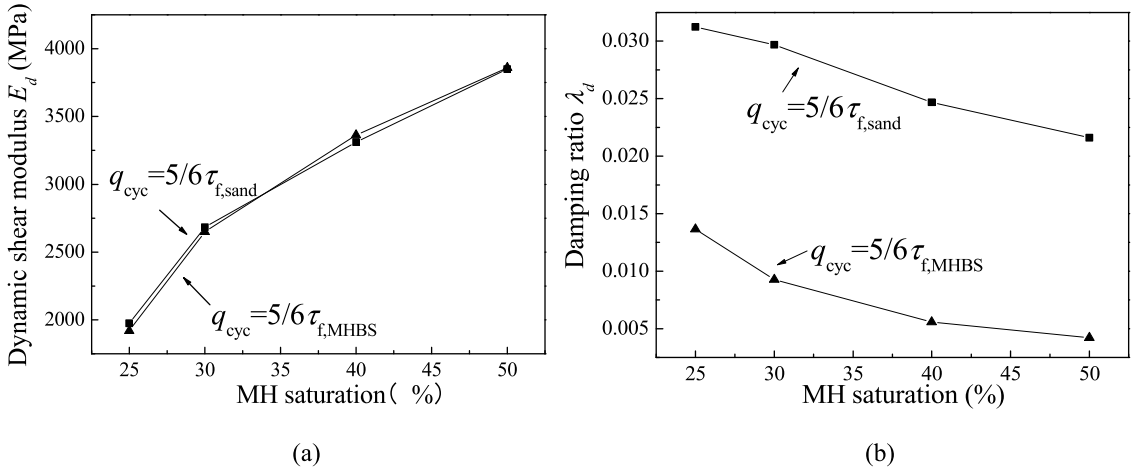

Fig. 18. Influence of different MH saturations on (a) E_d and (b) λ_d.

where A_b is the area of bond, A_v is the total void area, S_{MH_0} is the threshold value of hydrate saturation at which methane hydrates start to bond sand grains, A is the total area of the sample, e_p the sample planar void ratio, m is the total number of MH bonds in the sample, $A_{b,i}$ the area of each bond, $t_{0,i}$ the minimum thickness of each bond; more detailed principles for selecting these parameters can be found in [42].

The relationship between MH saturation and E_d and λ_d in Fig. 18 shows that when MH saturation increases, E_d increases significantly while λ_d decreases. The increase in q_{cyc} can lead to a decrease in λ_d, but there is no change in E_d. A larger mean strain rate means a larger damping force/moment. More work is done when the mean strain rate is larger. As the damping ratio indicates energy dissipation by damping under dynamic loading, the variation of the mean strain rate is the microscopic origin of the changes of the damping ratio.

Fig. 19 illustrates the influence of MH saturation on the mean strain rate of MH. Fig. 19 shows that the mean normal strain rate is always larger than the tangential one. When MH saturation increases, the mean normal strain rate obviously decreases, while the tangential one decreases slightly. In a fashion similar to the case in Fig. 17, the decrease of strain rate by the increasing MH saturation leads to the decrease of λ_d.

5.3.3. The influence of the initial effective confining pressure

As to the influence of initial effective confining pressure on E_d and λ_d, Fig. 20 shows that E_d increases rapidly when the initial effective confining pressure increases from 0.1 MPa to 1.0 MPa, while λ_d quickly decreases at the same time. However, when the initial effective confining pressure further increases from 1.0 MPa to 3.0 MPa, E_d and λ_d vary slowly. And it should be noted that the values of E_d and λ_d caused by $q_{cyc,sand}$ are larger than that caused by $q_{cyc,MHBS}$ at the same initial effective confining pressure. However, Fig. 21 shows that when the initial effective confining pressure increases, the mean normal strain rate increases nearly linearly and the tangential one increases slightly.

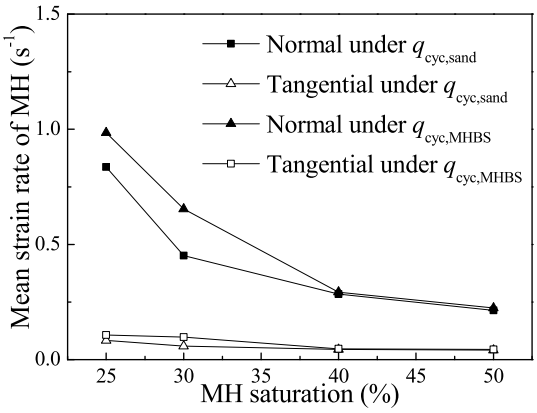

Fig. 19. Mean strain rate of MH under different MH saturations.

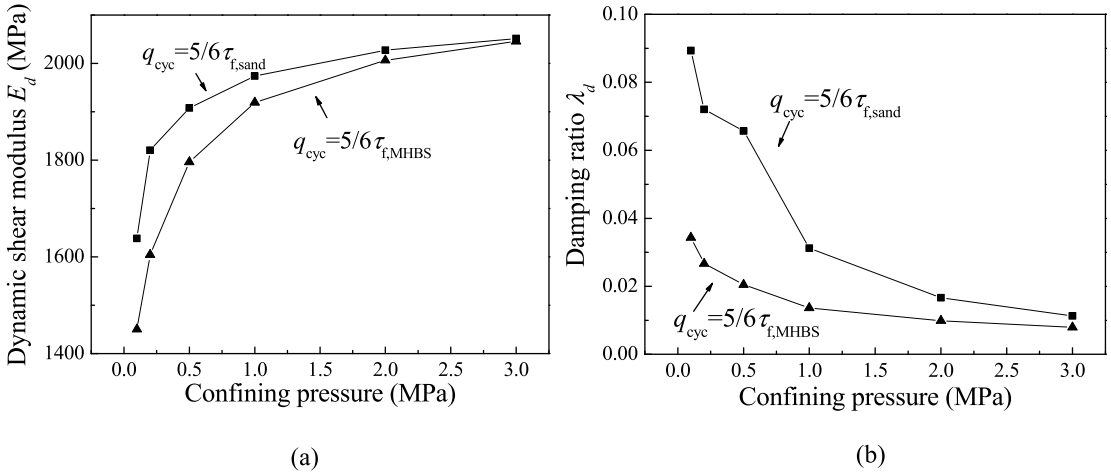

Fig. 20. Influence of confining pressure on (a) E_d and (b) λ_d.

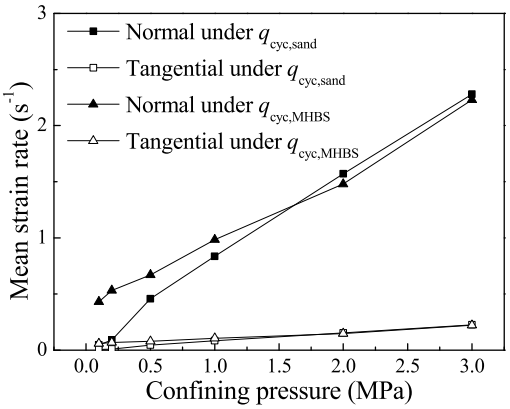

Fig. 21. Mean strain rate under different confining pressures.

6. Conclusions

This study proposed a 2D bond contact model incorporating the effect of the rate dependency of MH, and the contact model was implemented into the DEM software, PFC2D. A series of undrained cyclic biaxial tests were conducted to investigate the dynamic behavior of MHBS, and the test results were discussed with emphasis on stress–strain relationship, effective stress path, E_d and λ_d, along with the force chains, contact fabric, and averaged pure rotation rate (APR).

Finally, the influence of temperature, MH saturation and effective confining pressure on the dynamic behavior of MHBS was analyzed. The results showed that:

1) during the cyclic biaxial tests, the stress–strain relationship closed as a hysteretic loop after one cyclic load, the MHBS samples remained in the elastic state during the whole cyclic shearing due to the bonding effect of MH. The force chains, contact fabric, and APR seldom changed as a result of MH bonding;
2) E_{d} rapidly increased and λ_{d} quickly decreased when the initial effective confining pressure increased from 0.1 MPa to 1.0 MPa. When the initial effective confining pressure further increased from 1.0 MPa to 3.0 MPa, E_{d} and λ_{d} slowly varied. λ_{d} rarely varied, while E_d decreased almost in a linear way with increasing temperature. As to the influence of different MH saturations, E_{d} increased obviously, and λ_d decreased gradually when MH saturation increased;
3) microscopically, λ_{d} reflects the amount of energy dissipation caused by the viscous resistance, i.e. the increase in the strain rate of MH bonds can cause an increase in the damping ratio. However, this effect can be by hindered by the growing effective confining pressure.

Acknowledgements

This work is funded by the Major Project of Chinese National Programs for Fundamental Research and Development (973 Program) (2014CB046901), China National Funds (Nos. 51639008 and 51579178) and the 111 Project (No. B14017). All these supports are greatly appreciated.

References

[1] K.A. Kvenvolden, T.D. Lorenson, Global occurrences of gas hydrate, in: Proceedings of the 11th International Offshore and Polar Engineering Conference, Stavanger, Norway, 17–22 June 2001, 2001, pp. 462–467.
[2] R. Boswell, Is gas hydrate energy within reach?, Science 325 (2009) 957–958.
[3] R. Dawe, S. Thomas, A large potential methane source—natural gas hydrates, Energy Sources, Part A 29 (2007) 217–229.
[4] S.M. Lu, A global survey of gas hydrate development and reserves: specifically in the marine field, Renew. Sustain. Energy Rev. 41 (2015) 884–900.
[5] G. Ahmadi, C. Ji, D.H. Smith, Numerical solution for natural gas production from methane hydrate dissociation, J. Pet. Sci. Eng. 41 (2004) 269–285.
[6] K.A. Kvenvolden, Methane hydrate — a major reservoir of carbon in the shallow geosphere?, Chem. Geol. 71 (1988) 41–51.
[7] J.B. Klauda, S.I. Sandler, Global distribution of methane hydrate in ocean sediment, Energy Fuels 19 (2005) 459–470.
[8] H.E. Brown, W.S. Holbrook, M.J. Hornbach, J. Nealon, Slide structure and role of gas hydrate at the northern boundary of the Storegga Slide, offshore Norway, Mar. Geol. 229 (2006) 179–186.
[9] W.F. Waite, J.C. Santamarina, D.D. Cortes, B. Dugan, D.N. Espinoza, J. Germaine, M.J.R. Gee, H.S. Uy, J. Warren, C.K. Morley, J.J. Lambiase, The Brunei slide: a giant submarine landslide on the North West Borneo Margin revealed by 3D seismic data, Mar. Geol. 246 (2007) 9–23.
[10] M. Hyodo, Y.H. Li, J. Yoneda, Y. Nakata, N. Yoshimoto, A. Nishimura, Y.C. Song, Mechanical behavior of gas-saturated methane hydrate-bearing sediments, J. Geophys. Res., Solid Earth 118 (2013) 5185–5194.
[11] A. Masui, K. Miyazaki, H. Haneda, Y. Ogata, K. Aoki, Mechanical properties of natural gas hydrate bearing sediments retrieved from eastern Nankai trough, in: Offshore Technology Conference, Houston, TX, USA, 5–8 May, 2008.
[12] J.C. Santamarina, S. Dai, M. Terzariol, J. Jang, W.F. Waite, W.J. Winters, J. Nagao, J. Yoneda, Y. Konno, T. Fujii, K. Suzuki, Hydro-bio-geomechanical properties of hydrate-bearing sediments from Nankai Trough, Mar. Pet. Geol. 66 (2015) 434–450.
[13] W.J. Winters, I.A. Pecher, W.F. Waite, D.H. Mason, Physical properties and rock physics models of sediment containing natural and laboratory-formed methane gas hydrate, Am. Mineral. 89 (2004) 1221–1227.
[14] J. Yoneda, A. Masui, Y. Konno, Y. Jin, M. Kida, J. Katagiri, J. Nagao, N. Tenma, Pressure-core-based reservoir characterization for geomechanics: insights from gas hydrate drilling during 2012–2013 at the eastern Nankai Trough, Mar. Pet. Geol. 86 (2017) 1–16.
[15] M. Hyodo, J. Yoneda, N. Yoshimoto, Y. Nakata, Mechanical and dissociation properties of methane hydrate-bearing sand in deep seabed, Soil Found. 53 (2013) 299–314.
[16] Y.H. Li, Y.C. Song, W.G. Liu, F. Yu, R. Wang, X.F. Nie, Analysis of mechanical properties and strength criteria of methane hydrate-bearing sediments, Int. J. Offshore Polar Eng. 22 (2012) 290–296.
[17] K. Miyazaki, A. Masui, K. Aoki, Y. Sakamoto, T. Yamaguchi, S. Okubo, Strain-rate dependence of triaxial compressive strength of artificial methane-hydrate-bearing sediment, Int. J. Offshore Polar Eng. 20 (2010) 04.
[18] W.J. Winters, W.F. Waite, D.H. Mason, L.Y. Gilbert, I.A. Pecher, Methane gas hydrate effect on sediment acoustic and strength properties, J. Pet. Sci. Eng. 56 (2007) 127–135.
[19] J. Brugada, Y.P. Cheng, K. Soga, J.C. Santamarina, Discrete element modelling of geomechanical behaviour of methane hydrate soils with pore-filling hydrate distribution, Granul. Matter 12 (2010) 517–525.
[20] J.W. Jung, J.C. Santamarina, K. Soga, Stress–strain response of hydrate-bearing sands: numerical study using discrete element method simulations, J. Geophys. Res., Solid Earth 117 (2012) B04202.
[21] Z.F. Shen, M.J. Jiang, DEM simulation of bonded granular material. Part II: extension to grain-coating type methane hydrate bearing sand, Comput. Geotech. 75 (2016) 225–243.
[22] S. Uchida, K. Soga, K. Yamamoto, Critical state soil constitutive model for methane hydrate soil, J. Geophys. Res., Solid Earth 117 (2012) B3.
[23] C.R.I. Clayton, J.A. Priest, A.I. Best, The effects of disseminated methane hydrate on the dynamic stiffness and damping of a sand, Geotechnique 55 (2005) 423–434.
[24] J.Y. Lee, F.M. Francisca, J.C. Santamarina, C. Ruppel, Parametric study of the physical properties of hydrate-bearing sand, silt, and clay sediments: 2. Small-strain mechanical properties, J. Geophys. Res., Solid Earth 15 (2010) B11.
[25] J.A. Priest, A.I. Best, C.R.I. Clayton, Attenuation of seismic waves in methane gas hydrate-bearing sand, Geophys. J. Int. 164 (2006) 149–159.
[26] T.S. Yun, F.M. Francisca, J.C. Santamarina, C. Ruppel, Compressional and shear wave velocities in uncemented sediment containing gas hydrate, Geophys. Res. Lett. 32 (2005) 20.
[27] Y. Zhu, Y. Li, W. Liu, Y. Song, T. Luo, Z. Wu, Dynamic strength characteristics of methane hydrate-bearing sediments under seismic load, J. Nat. Gas Sci. Eng. 26 (2015) 608–616.
[28] P. De Alba, C.K. Chan, H.B. Seed, Determination of Soil Liquefaction Characteristics by Large-scale Laboratory Tests, Earthquake Engineering Research Center, University of California, CA, USA, 1975.

[29] K. Sell, E.H. Saenger, A. Falenty, M. Chaouachi, D. Haberthür, F. Enzmann, W.F. Kuhs, M. Kersten, On the path to the digital rock physics of gas hydrate-bearing sediments-processing of in situ synchrotron-tomography data, Solid Earth 7 (2016) 1243–1258.
[30] P.A. Cundall, O.D. Strack, A discrete numerical model for granular assemblies, Geotechnique 29 (1979) 47–65.
[31] N. Guo, J. Zhao, Local fluctuations and spatial correlations in granular flows under constant-volume quasistatic shear, Phys. Rev. E 89 (2014) 042208.
[32] T.G. Sitharam, S.V. Dinesh, N. Shimizu, Micromechanical modelling of monotonic drained and undrained shear behaviour of granular media using three-dimensional DEM, Int. J. Numer. Anal. Methods Geomech. 26 (2002) 1167–1189.
[33] C. Thornton, D.J. Barnes, Computer simulated deformation of compact granular assemblies, Acta Mech. 64 (1986) 45–61.
[34] J.D. Zhao, T. Shan, Coupled CFD–DEM simulation of fluid–particle interaction in geomechanics, Powder Technol. 239 (2013) 248–258.
[35] J. Zhou, Z. Wang, X. Chen, J. Zhang, Uplift mechanism for a shallow-buried structure in liquefiable sand subjected to seismic load: centrifuge model test and DEM modeling, Earthq. Eng. Eng. Vib. 13 (2014) 203–214.
[36] M.J. Jiang, C. Sun, G.B. Crosta, W.C. Zhang, A study of submarine steep slope failures triggered by thermal dissociation of methane hydrates using a coupled CFD–DEM approach, Eng. Geol. 190 (2015) 1–16.
[37] M. Hyodo, A.F.L. Hyde, Y. Nakata, N. Yoshimoto, M. Fukunaga, K. Kubo, Y. Nanjo, T. Matsuo, K. Nakamura, Triaxial compressive strength of methane hydrate, in: Proceedings of the 12th International Offshore and Polar Engineering Conference, Kitakyushu, Japan, 26–31 May 2002, 2002, pp. 422–428.
[38] Y. Nabeshima, Y. Takai, T. Komai, Compressive strength and density of methane hydrate, in: Proceedings of the ISOPE (International Society of Offshore and Polar Engineers) Ocean Mining Symposium, 2005, pp. 199–202.
[39] K. Miyazaki, A. Masui, Y. Sakamoto, N. Tenma, T. Yamaguchi, Effect of confining pressure on triaxial compressive properties of artificial methane-hydrate-bearing sediments, in: Proc. 2010 Offshore Technology Conference, Houston, TX, USA, 3–6 May, 2010.
[40] K. Miyazaki, N. Tenma, Y. Sakamoto, T. Yamaguchi, S. Okubo, Effects of methane hydrate saturation and confining pressure on strain-rate dependence of artificial methane-hydrate-bearing sediment in triaxial compression test, Int. J. Offshore Polar Eng. 22 (2012) 01.
[41] K. Miyazaki, E. Yoshihiro, N. Tenma, T. Yamaguchi, Sand grain size dependence of viscoelastic properties of artificial methane-hydrate-bearing sediment sample, in: Proc. 24th International Ocean and Polar Engineering Conference, Busan, Korea, 15–20 June, International Society of Offshore and Polar Engineers, 2014.
[42] M.J. Jiang, F.Y. Zhu, F. Liu, S. Utili, A bond contact model for methane hydrate-bearing sediments with interparticle cementation, Int. J. Numer. Anal. Methods Geomech. 38 (2014) 1823–1854.
[43] M.J. Jiang, J. He, J.F. Wang, B. Chareyre, F.Y. Zhu, DEM analysis of geomechanical properties of cemented methane hydrate-bearing soils at different temperatures and pressures, Int. J. Geomech. 16 (2015) 04015087.
[44] M.J. Jiang, Y.G. Sun, L.Q. Li, H.H. Zhu, Contact behavior of idealized granules bonded in two different interparticle distances: an experimental investigation, Mech. Mater. 55 (2012) 1–15.
[45] M.J. Jiang, Y.G. Sun, Y. Xiao, An experimental investigation on the mechanical behavior between cemented granules, Geotech. Test. J. 35 (2012) 678–690.
[46] M. Hyodo, Y. Nakata, N. Yoshimoto, T. Ebinuma, Basic research on the mechanical behavior of methane hydrate-sediments mixture, Soil Found. 45 (2005) 75–85.
[47] Y.C. Song, F. Yu, Y.H. Li, W. Liu, J.F. Zhao, Mechanical property of artificial methane hydrate under triaxial compression, J. Nat. Gas Chem. 19 (2010) 246–250.
[48] F. Yu, Y.C. Song, W.G. Liu, Y.H. Li, J.F. Zhao, Study on shear strength of artificial methane hydrate, in: Proc. ASME 2010, 29th International Conference on Ocean, Offshore and Arctic Engineering, ASME, Shanghai, China, 6–11 June, 2010.
[49] Y. Li, Equation of state of water and sea water, J. Geophys. Res. 72 (1967) 2665–2678.
[50] S. Ergun, Fluid flow through packed columns, Chem. Eng. Prog. 48 (1952) 89–94.
[51] C.Y. Wen, Y.H. Yu, A generalized method for predicting the minimum fluidization velocity, AIChE J. 12 (1966) 610–612.
[52] M.J. Jiang, J.M. Konrad, S. Leroueil, An efficient technique for generating homogeneous specimens for DEM studies, Comput. Geotech. 30 (2003) 579–597.
[53] J. Zhou, Y.X. Yang, Y. Liu, M.C. Jia, Numerical modeling of sand liquefaction behavior under cyclic loading, Ser. Rock Soil Mech. 30 (2009) 1083–1088.
[54] M.J. Jiang, H.S. Yu, D. Harris, Bond rolling resistance and its effect on yielding of bonded granulates by DEM analyses, Int. J. Numer. Anal. Methods Geomech. 30 (2006) 723–761.
[55] C. Thornton, S.J. Cummins, P.W. Cleary, An investigation of the comparative behaviour of alternative contact force models during inelastic collisions, Powder Technol. 233 (2013) 30–46.
[56] B. Imre, S. Rabsamen, S. Springman, A coefficient of restitution of rock materials, Comput. Geosci. 34 (2003) 339–350.
[57] M. Hyodo, H. Murata, N. Yasufuku, T. Fujii, Undrained cyclic shear strength and residual shear strain of saturated sand by cyclic triaxial tests, Soil Found. 31 (1991) 60–76.
[58] M.J. Jiang, H.S. Yu, D. Harris, Kinematic variables bridging discrete and continuum granular mechanics, Mech. Res. Commun. 33 (2006) 651–666.